ADVANCED FUNCTIONAL MATERIALS
www.afm-journal.de

Direct Organometallic Synthesis of Carboxylate Intercalated Layered Zinc Hydroxides for Fully Exfoliated Functional Nanosheets

Said A. Said, Christopher S. Roberts, Ja Kyung Lee, Milo S. P. Shaffer, and Charlotte K. Williams**

Intercalation of organic anions into 2D materials can enable exfoliation, improve dispersion stability, increase surface area, and provide useful functional groups. In layered metal hydroxides, intercalation of bulk structures is commonly achieved by cumbersome and typically incomplete anion exchange reactions. In contrast, here, a series of carboxylate-intercalated layered zinc hydroxides (LZH-R) are synthesized directly, at room temperature, by reacting an organozinc reagent with a precise sub-stoichiometric quantity of the desired carboxylic acid and water. A range of carboxylic acids are used to make new LZH-R materials which are crystalline, soluble, and functionalized, as established by X-ray diffraction, spectroscopic, and microscopy techniques. When R is an alkyl ether carboxylate, this direct synthesis method results in the spontaneous exfoliation of the LZH-R into monolayer nanosheets with high yields (70–80%) and high solubilities in alcohols and water of up to 180 mg mL^{-1}. By altering the carboxylate ligand, functional groups suitable for post-synthetic modification or for detection by fluorescence are also introduced. These examples demonstrate a versatile synthetic route for functional exfoliated nanosheets.

1. Introduction

Layered metal hydroxides are an important class of materials, comprising an inorganic framework combined with a wide range of intercalating anions. Under certain conditions, the intrinsically anisotropic crystal structure can be exfoliated to form 2D nanomaterials. The nature of the intercalating anion is critical in determining both the extent of exfoliation and the subsequent solubility or stability in solvent. Liquid phase processing is a crucial processing route to deliver inorganic–organic hybrids, single-component nanocomposites, catalysts and support materials, excipients for drug delivery, energy storage materials, active layers in optoelectronic devices and sorbents.[1] Layered zinc hydroxides (LZHs) with the formula $[Zn_5(OH)_8(A^{n-})_{2/n}\cdot mH_2O]$ exhibit Brucite-like structures, consisting of planes of edge-sharing $Zn(OH)_6$ octahedra where a quarter of sites are replaced by $Zn(OH)_3A$ tetrahedra located above and below the plane (**Figure 1**a).[2] The anions (A^{n-}), may be uncoordinated (as is typical for inorganic anions) or coordinated at the tetrahedral apex (as is typical for organic anions).[3] These LZHs are used in catalysis,[4] for the encapsulation of anionic dyes,[5] and in active molecule delivery,[6] as well as providing important precursors to porous zinc oxide films and other nanostructures.[7] Zinc oxide is a well-known *n*-type semiconductor sought for its optical transparency, high electron mobility, biocompatibility, and room-temperature luminescence.[8]

LZHs, and other layered metal hydroxides, are commonly synthesized by salt co-precipitations, hydrothermal methods, or by the hydrolyses of inorganic salts.[9] Following their preparation, the LZHs must be subsequently subjected to anion-exchange reactions to replace anions such as nitrate, carbonate, sulphate, and halides with the desired organic or functional species (Figure 1b).[10] The exchange reactions typically require a large excess of organic anion, high temperatures, and prolonged reaction times. These reaction conditions compromise the efficiency of the organic anion intercalation and result in undesirable mixtures. Moreover, layered metal hydroxides are prone to contamination by carbonates, either directly from the synthesis or due to adventitious reaction with atmospheric carbon dioxide. Such carbonates are very difficult to completely remove as they are strongly coordinated in the interlayer galleries, and attempts to remove them typically involve multi-stage sequences of anion exchange.[11]

S. A. Said, Prof. C. K. Williams
Chemistry Research Laboratory
University of Oxford
12 Mansfield Road, Oxford OX1 3TA, UK
E-mail: charlotte.williams@chem.ox.ac.uk
Dr. C. S. Roberts, Dr. J. K. Lee, Prof. M. S. P. Shaffer
Molecular Sciences Research Hub (MSRH)
Department of Chemistry
Imperial College London
82 Wood lane, London SW7 2AZ, UK
E-mail: m.shaffer@imperial.ac.uk
Prof. M. S. P. Shaffer
Department of Materials
Imperial College London
London SW7 2AZ, UK
The ORCID identification number(s) for the author(s) of this article can be found under https://doi.org/10.1002/adfm.202102631.

DOI: 10.1002/adfm.202102631

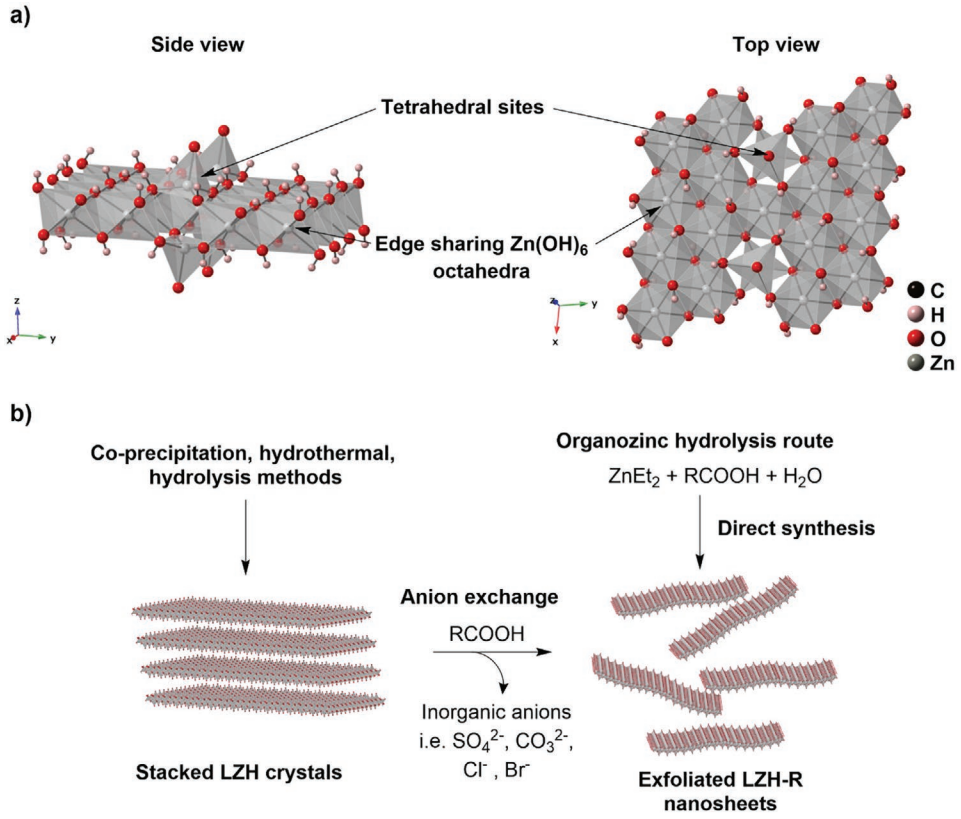

Figure 1. a) Model of the LZH structure along the *ab* plane (right) and along the *c* axis (left). b) Illustration of conventional routes requiring subsequent anion exchange reactions versus the direct organozinc route to carboxylate intercalated LZH, described in this work.

The difficulties in anion exchange processes limit both the extent and yield of the exfoliation into discrete monolayers of soluble nanosheets. Exfoliation, therefore, is almost always aided by energy intensive methods, typically ultra-sonication, high-shear ball milling, and homogenization, and/or the use of a small selection of chemical exfoliating agents or reflux in specialist solvents such as formamide. A better approach would be to develop the direct syntheses of organic anion intercalated layered metal hydroxides in order to both circumvent the need for anion exchange steps and deliver materials soluble in a broader range of solvents.[12]

Soluble zinc oxide nanoparticles can be synthesized by the hydrolysis of organozinc reagents in the presence of substoichiometric quantities of ligands.[13] These organometallic syntheses are conducted in organic solvents, at room temperature and deliver crystalline ZnO particles which are coordinated by ligands such as carboxylates, amines, and phosphinates.[14] In particular, using non-hydrolysable zinc carboxylates or phosphinates delivers small ZnO nanoparticles, with diameters in the range 3–5 nm, which show high solubility in various organic solvents.[15] In 2018, our group applied a related organozinc hydrolysis method to make LZH nanosheets: the hydrolysis of diethyl zinc in the presence of alkyl zinc carboxylate complexes produced a series of alkyl carboxylate intercalated LZH.[16] The oleate-intercalated LZH nanosheets showed good solubility in toluene. Here, we aim to transform this initial result into a general principle, showing that exfoliated LZHs can be rendered both functional and soluble in a range of solvents, including common polar solvents such as ethanol and water. To increase polarity, the strategy is to use carboxylate ligands featuring hydrophilic alkyl ether chains. Polar-solvent exfoliated inorganic nanomaterials are important for future applications where volatile organic solvents are not desirable, such as chemical catalysis using water soluble substrates, production of biopolymer composites, and as inks for large-scale printing of nanostructured thin-films for photo-, electrocatalysis, or optoelectronic devices.[17] In addition to improving solubility, the ligands can be designed to add function to the LZHs, directly, without the size, diffusion, and selectivity/affinity constraints associated with anion exchange methods. As proof of principle, functional carboxylic acids containing a terminal vinyl group (i.e., 5-hexenoate) or a photoluminescent unit (i.e., 9-anthracenecarboxylate) are also introduced to demonstrate functionally relevant properties.

2. Results and Discussion

2.1. LZH Synthesis

The carboxylate-intercalated LZH-R materials, where R^1–n = alkyl ether chains, $-O_2C(CH_2O((CH_2)_2O)_nCH_3$ (n = 0, 1, 2, and 4), R^2 = 5-hexenoate and R^3 = 9-anthracenecarboxylate, were synthesized by modifying the previously reported synthesis (**Scheme 1**).[16] Diethyl zinc was added to a solution of the appropriate carboxylic acid at a molar ratio of [COOR]/[Zn] of

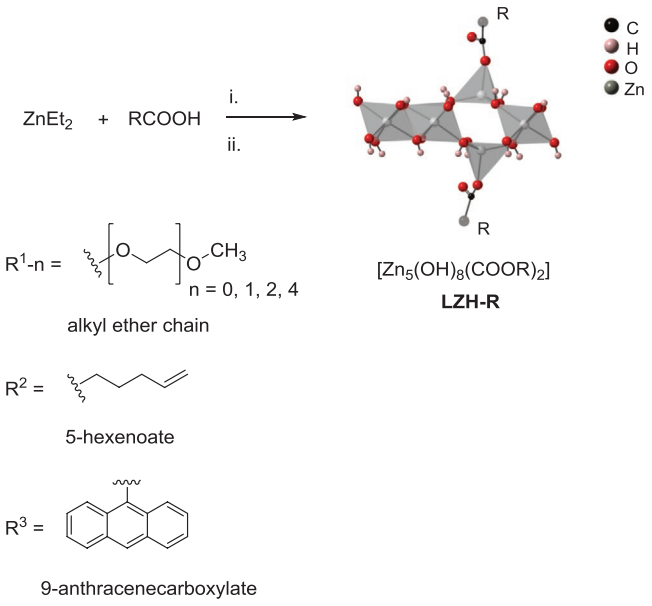

Scheme 1. Synthesis of the LZH-R materials (with the repeat unit illustrated) by the controlled hydrolysis of diethyl zinc with 0.6 equiv. of carboxylic acid. Reagents and conditions: i. Toluene, 20 °C, 16 h, ii. Toluene, 1.6 equiv. of H_2O, 20 °C, 3 h.

0.6; a slight excess of the acid is added relative to the stoichiometry of $[Zn_5(OH)_8A_2]$ ([A]/[Zn] = 0.4) to deliver the LZH free from any detectable zinc oxide. The reaction between diethyl zinc and carboxylic acids proceeds via the formation of pentanuclear clusters, $[Zn_5(Et)_4(COOR)_6]$, with the excess diethyl zinc rapidly exchanging with the coordinated zinc ethyl groups.[18] Both the cluster and excess diethyl zinc were identified in the ^{1}H NMR spectrum of the reaction mixture used to prepare LZH-R^1-1 (Figure S1, Supporting Information). The reaction mixture was then hydrolyzed using stoichiometric amounts of water (1.6 equiv. relative to zinc), at room temperature. The entire synthesis was conducted under a nitrogen atmosphere to prevent any zinc carbonate or oxygen insertion side-reactions. The cluster and excess diethyl zinc react rapidly and irreversibly with water to form the LZH material, gradually forming translucent solutions in the case of LZH-R^1-n and -R^2, and a yellow powder in the case of -R^3. The final materials were isolated by centrifugation and dried under reduced pressure; further purification was unnecessary since the only by-product of the synthesis is ethane gas which is easily dissipated. The LZH-R were obtained in quantitative yields based on the starting zinc complex. The LZHs obtained in this synthesis, may be considered to be kinetic products since they efficiently decompose to ZnO upon gentle heating (>40 °C).

2.2. Characterization

The powder X-ray diffraction (XRD) patterns confirm the formation of LZH, identified by characteristic, equally spaced (00*l*), *l* = 1, 2, 3, etc., basal reflections at low 2θ (<20°), free from ZnO contamination or other by-products (**Figure 2**a). As expected, the (00*l*) peaks in the LZH-R^1-n series become more closely spaced and shift toward lower 2θ with increasing chain length, reflecting a progressive increase in the basal spacing (**Table 1** and Figure S2, Supporting Information). The intense (00*l*) reflections likely arise from preferential orientation as well as high order stacking. This texture effect is particularly

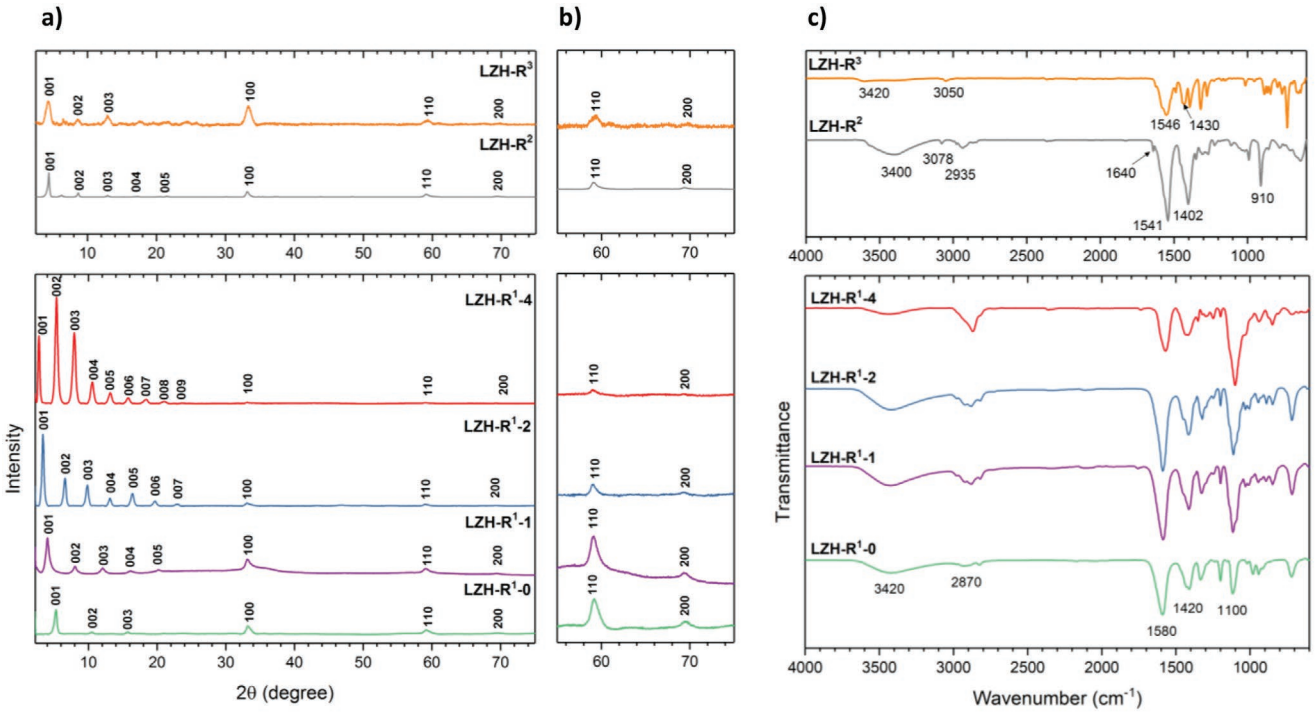

Figure 2. LZH-R characterization data: a) XRD patterns, b) magnified XRD region of 55–75° 2θ and c) FTIR spectra.

Table 1. Measured values for interlayer spacing of LZHs and respective Zn content from thermal gravimetric analysis (TGA) data.

	Basal spacing calculated from XRD [nm][a)]	Basal spacing observed by AFM [nm][b)]	Experimental Zn content [wt%][c)]	Theoretical Zn content [wt%][d)]
LZH-R^1-0	1.7 ± 0.02	–	51	51
LZH-R^1-1	2.19 ± 0.02	2.21 ± 0.24	36	38
LZH-R^1-2	2.65 ± 0.03	5.26 ± 0.22	31[c)]	33
LZH-R^1-4	3.33 ± 0.07	3.45 ± 0.21	23	25
LZH-R^2	2.06 ± 0.03	–	38[c)]	39
LZH-R^3	2.07 ± 0.02	–	28	29

[a)]Calculated using the Bragg equation for (00*l*) reflections; [b)]Height profiles of exfoliated monolayers measured by AFM; [c)]Determined from TGA data (error approx. ±3 wt%); [d)]Presence of 1 equiv. excess of carboxylate anion accounted for in the calculation.

striking for LZH-R^1-2 and -4, which exhibit wax-like properties. In comparison, the LZH-R^2 and LZH-R^3 XRD patterns show fewer and less intense (00*l*) reflections associated with the increase in random orientation for these powder samples. Other characteristic LZH peaks are observed at 33, 59 and 69° 2θ corresponding to the (100), (110), and (200) in-plane reflections, respectively (Figure 2b and Figure S3, Supporting Information). These in-plane reflections were more pronounced than the (00*l*) reflections for LZH-R^2 and LZH-R^3 and the associated asymmetric broadening is attributed to turbostratic disorder which is common to layered materials.[19]

The stacking behavior observed for some of the LZH during drying was examined using time-resolved XRD, applied to an as-synthesized solution of LZH-R^1-4 (Figure S4, Supporting Information). The XRD data indicates the progressive stacking of LZH by the appearance and increasing intensity of the (00*l*) reflections with drying, suggesting the formation of stacks from discrete layers. The decrease in average basal spacing from ≈4 to 3.3 nm further suggests that an optimal interlayer arrangement of LZH-R^1-4 is achieved once the solvent is completely removed.

The Fourier-transform infrared (FTIR) spectra show characteristic broad O—H stretches observed at ≈3400 cm^{-1} (Figure 2c). The coordination of carboxylate ligand to the zinc is confirmed by asymmetric and symmetric carboxylate stretches at 1550 and 1430 cm^{-1}, respectively. The coordinated carboxylate stretching frequencies are clearly distinguished from those of the carboxylic acid, at 1750 (C=O) and 2880 cm^{-1} (O—H). Various other peaks confirm the presence of the organic anions including, 2870 (C—H) and 1100 cm^{-1} (C—O—C) stretches in the LZH-R^1-n series; 3078 (=C—H) and 910 cm^{-1} (C=C) stretches for LZH-R^2; and 3050 cm^{-1} (=C—H) for LZH-R^3. The spectroscopic data are consistent with other carboxylic acid intercalated layered metal hydroxides.[20]

The thermal degradation of the LZH, in air, was examined by thermal gravimetric analysis coupled with differential thermal analysis (TGA-DTA) and mass spectrometry (TGA-MS) (Figures S5 and S6, Supporting Information). The TGA data show the expected degradation profiles with two distinct transitions commonly observed for layered metal hydroxides.[21] The initial mass loss, at ≈100 °C, corresponds to the release of surface adsorbed and interlayer water molecules as evidenced by the endothermic transition and the detection of ions corresponding to m/z 18. The second and larger mass loss occurs at temperatures above 200 °C and is assigned to the simultaneous dehydroxylation and decomposition of the intercalating ligand as evidenced by the large exothermic transition as well as the detection of gases evolving from the decomposition of alkyl ether moieties. The evolved gases were consistent for all the LZH-R^1-*n* series, with m/z peaks corresponding to H_2O (18), CH_3^+ (15), CO_2 (44), and $CH_3O—CH_2$/COOH (45). The Zn content (wt%), calculated from the final weight was in good agreement with the calculated values for $[Zn_5(OH)_8(COOR)_2]$ (Table 1). The stoichiometry was further confirmed by elemental analyses for all LZH-R (Experimental Section).

The morphologies of the dried solid LZH-R were investigated by scanning electron microscopy (SEM, Figure S7, Supporting Information). Images of LZH-R^1-0, -R^1-1, -R^2, and -R^3 reveal typical crystallites of flake-like material. In contrast, images of the drop-cast samples of LZH-R^1-1, -R^1-2, and -R^1-4 show morphologies that are more consistent with lamellar-like microstructures observed in films of extended layers.[22]

2.3. Solubility and Exfoliation of LZH-R^1-*n*

The solubility of the LZH-R^1-*n* series was assessed by gentle shaking or stirring in solvents with increasing polarity including ethyl acetate, ethanol, methanol and water. As expected, LZH-R^1-0 was found to have negligible solubility in any of these solvents (<5 mg mL^{-1}) and therefore was not further investigated in terms of exfoliation. However, LZH-R^1-*n* (*n* = 1, 2, and 4) formed transparent colloidal solutions in dry ethyl acetate, ethanol, methanol, and water, and showed increasing solubility with alkyl ether chain length and solvent polarity (Table S1, Supporting Information). Tyndall scattering from the transparent solutions indicate the formation of colloidal solutions of exfoliated layers (Figure S8, Supporting Information).[23] Accordingly, LZH-R^1-4 provided the highest solubilities in this series with concentrations reaching 18, 30, 75, and 180 mg mL^{-1} for ethyl acetate, ethanol, methanol, and water, respectively. In contrast to the exfoliation conditions necessary for other layered metal hydroxides, neither prolonged stirring, sonication, or heating were required to achieve spontaneous dissolution in these solvents. The maximum solubility values exceed by an order of magnitude any previous reports for LZH or related layered double hydroxides (LDHs) in polar solvents, including samples intercalated with dodecyl sulfate in 1-butanol or formamide (Table S2, Supporting Information).[24] Advancing our previous work, LZHs can be exfoliated in both apolar and polar solvents with much higher solubility; achieving this outcome relies upon appropriate ligand selection and the use of the direct organometallic synthesis.

The exfoliated solutions of LZH-R^1-1, –2 and –4 in ethyl acetate, ethanol, and methanol displayed good stability for over the course of a week with no precipitation. The XRD patterns of drop-cast aliquots confirmed that the LZH reflections were retained and no zinc oxide formed (Figures S9–S11, Supporting Information). These drop-cast solutions produced highly oriented films, with a strong texture effect, as already noted with SEM. Aqueous solutions of LZH-R^1-0, –1, and –2 decomposed,

likely via the condensation of $Zn(OH)_2$, to give zinc oxide species over the course of a week, as confirmed by XRD (Figures S12–S14, Supporting Information).[25] In contrast, aqueous solution of LZH-R^1-4 formed a stable translucent hydrogel. The XRD pattern of the gel shows the loss of the sharp (00*l*) reflections, whilst in-plane reflections are retained, consistent with the formation of exfoliated nanosheets (Figure S15, Supporting Information). The reappearance of the (00*l*) reflections in the XRD upon drying the gel without any ZnO formation, shows that the longest stabilizing chain (LZH-R^1-4) prevents the condensation in water. The gelation may be a consequence of the high aspect ratio of the soluble LZH-R^1-4, akin to similar effects observed for solvated surfactant intercalated layered double hydroxides.[26]

To assess the degree of exfoliation of these samples, dilute colloidal dispersions of LZH-R^1-*n* (*n* = 1, 2, and 4, ≈0.05 mg mL^{-1}, in methanol) were deposited on silicon wafers, and imaged using atomic force microscopy (AFM, **Figure 3**). All three samples reveal highly exfoliated individual nanosheets with varying lateral sizes of fifty to several hundred nanometers. The topography (height profile) measurements for LZH-R^1-1 show complete exfoliation down to individual monolayers, with an average

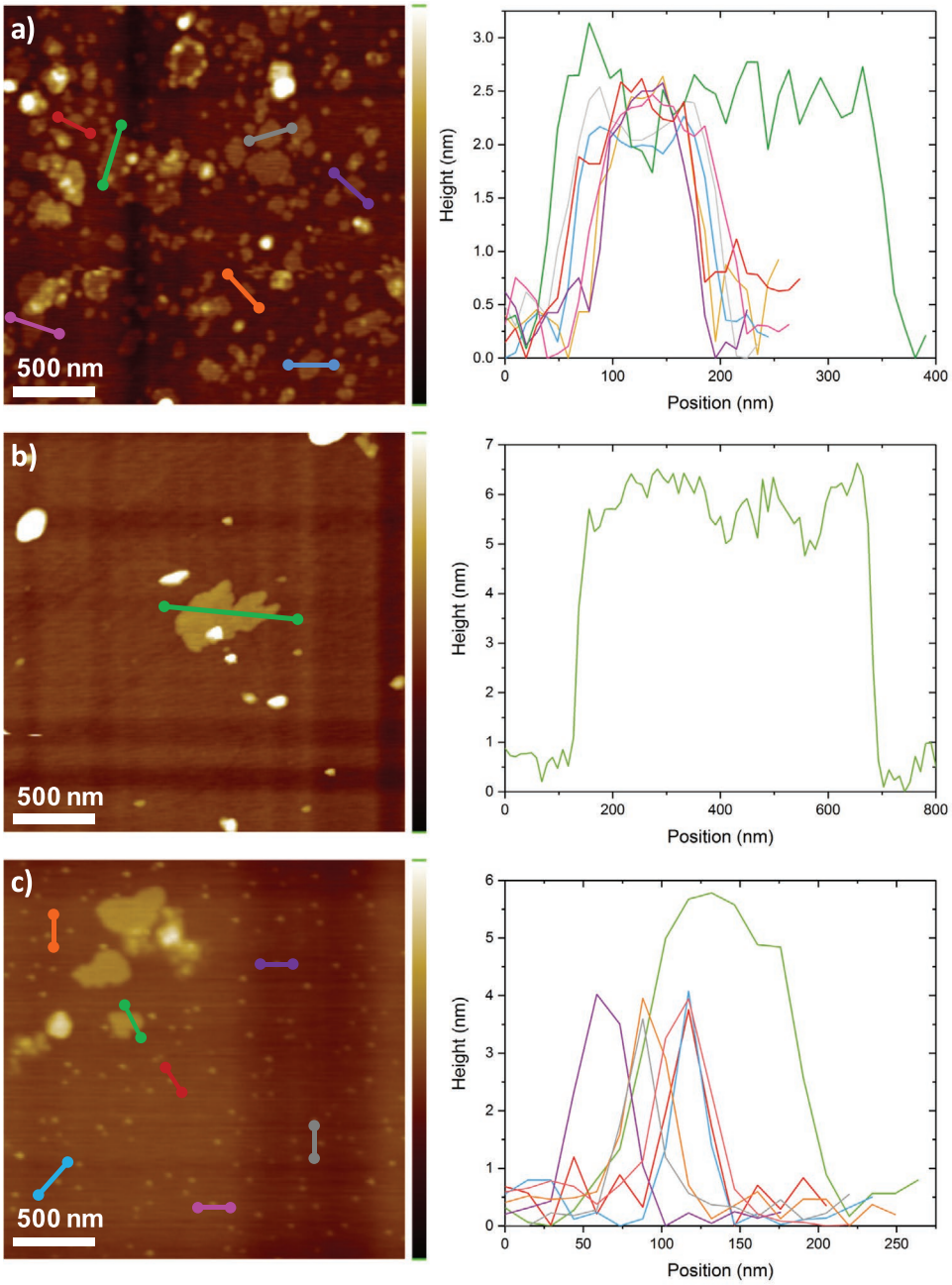

Figure 3. AFM images of exfoliated nanosheets deposited onto Si substrate; a) LZH-R^1-1, b) LZH-R^1-2 and c) LZH-R^1-4 with corresponding height profiles of the exfoliated nanosheets (right).

thickness of 2.21 ± 0.24 nm, consistent to the basal spacing of 2.19 ± 0.02 nm obtained by XRD (Figure 3a). Intriguingly, LZH-R^1-2 exfoliated predominately to bilayer nanosheets, with height profiles averaging double (5.26 ± 0.22 nm) the XRD basal spacing of 2.65 ± 0.03 nm (Figure 3b). The exfoliation of LZH-R^1-4 yielded a height profile of 3.45 ± 0.21 nm again consistent with the exfoliation to monolayer nanosheets (Figure 3c). The LZH-R^1-4 nanosheets consist of a high proportion of noticeably smaller lateral sizes (≈50–100 nm). One plausible reason for the smaller nanosheets of LZH-R^1-4 is that the long alkyl ether chains may hinder lattice growth, through oriented attachment (vide infra). Similar effects of anion size on the nanosheet growth have previously been reported for adamantane carboxylate intercalated LDHs which were also found to give small lateral sizes.[27] The yields of exfoliated nanosheets were determined by the distribution of layer thickness to give the relative proportion of monolayers, bilayers, trilayers, and multilayers (Figures S16–S18, Supporting Information). The exfoliated nanosheets of LZH-R^1-1 and LZH-R^1-4 exhibit appreciably high monolayer yields of ≈70–80%, respectively (Table S3, Supporting Information). In contrast, the exfoliated nanosheets of LZH-R^1-2 exhibit a high bilayer yield of 80%.

Transmission electron microscopy (TEM) analysis reveals further evidence of individual exfoliated nanosheets as well as the presence of stacking in LZH-R^1-n (n = 1, 2, and 4). All TEM experiments were carefully conducted on several sample sets with an accelerating voltage of 80 kV to reduce the electron-beam-induced degradation of the LZH nanosheets.[28] High-resolution TEM revealed areas of an *ab*-oriented LZH-R^1-1 monolayer showing lattice fringes corresponding to (100) reflections (d = 0.270 ± 0.001 nm), which is easily distinguished from the lattice fringes observed in some areas where decomposition to ZnO nanoparticles had occurred (Figure S19a,b, Supporting Information). Interestingly, the monolayer nanosheets, which are distinguishable from multilayer regions, consisted of several crystalline nano-domains of (100) lattice fringes in LZH-R^1-1 samples (Figure S19c,d, Supporting Information). The color-coded dark-field TEM image reconstructed from the (100) peaks, shows that each nano-domain exhibits different in-plane orientations, which is indicative of nanosheet controlled growth via a 2D oriented attachment mechanism (**Figure 4**).[29] The detailed growth mechanism and the relationships between the final structures and in-plane orientations between neighboring nano-domains warrant further investigation in future.

The TEM images of exfoliated samples of LZH-R^1-1, -2, and -4 show nanosheets with lateral sizes consistent with AFM measurements (**Figure 5**a–c). Scanning TEM (STEM) images further confirm the extended nature of the individual nanosheets within concentrated areas, consistent with the SEM images of drop-cast samples (Figure S20, Supporting Information). LZH-R^1-n were also present as stacks with equally spaced layers in areas of agglomerated material (Figure 5d–f). When oriented with the layers perpendicular (side-on) to the incident electron beam, these stacks show clear fringes with measured distances corresponding to the basal spacings of the (001) reflections. LZH-R^1-1 shows several stacks, consisting of ≈3–6 individual layers, with the enlarged view clearly showing side-on stacking (Figure 5d,g). The measured average interlayer spacing of 2.53 ± 0.51 nm, measured from several stacks, was consistent with the basal spacings determined by XRD (2.19 ± 0.02 nm), within error. Similar TEM observations of side-on orientated stacks of LZHs have been reported in previous studies.[30] On the other hand, stacks of laterally larger LZH layers were observed at tilted orientations relative to the TEM grids in samples of LZH-R^1-2 and -4. These tilted stacks are distinguishable from side-on stacks along the *ab*-plane using intensity profiling (Figure S21, Supporting Information). The presence of tilted orientations in these stacks accounts for the larger than expected apparent interlayer spacings of 3.64 ± 2.35 nm measured in LZH-R^1-2 compared to the XRD basal spacing of 2.65 ± 0.03 nm (Figure 5e,h). LZH-R^1-4 shows regions of both tilted and side-on stacking (Figure 5f,i). The apparent interlayer spacing measured in the titled region was 6.94 ± 1.24 nm, whereas that measured for the perpendicular region was 3.58 ± 0.26 nm which is consistent with the XRD basal spacing of 3.33 ± 0.07 nm (inset, Figure 5i).

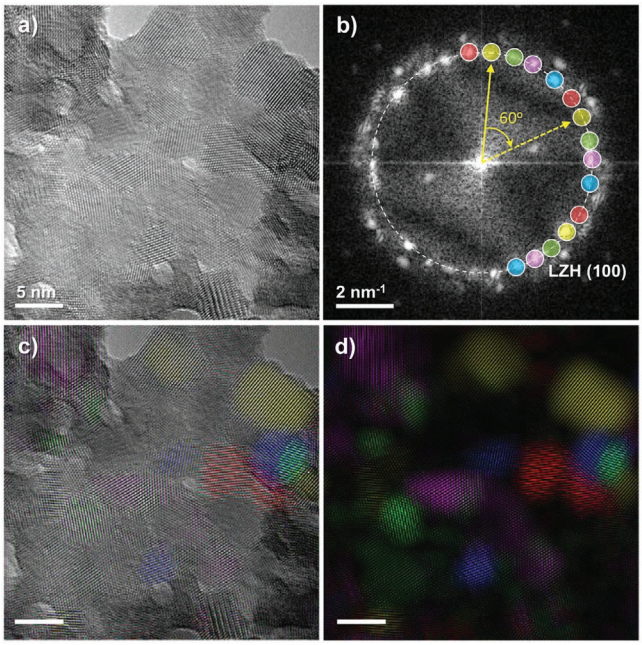

Figure 4. Bright-field HRTEM image of a) LZH-R^1-1 monolayer nanosheet consisting of nano-domains with different in-plane orientations and b) the corresponding FFT pattern highlighting the (100) diffraction spots along the white dotted circle. False color images of the virtual dark-field TEM image were reconstructed using an IFFT calculation on the (100) diffraction spots with applied spatial masks. Diffraction spots corresponding to hexagonal symmetry (i.e., consisting of 60× n-degrees relationship, n = integer) are coded with the same color and five different in-plane orientations are observed which are cultured red, yellow, green, pink, blue. c) Color-coded overlay of the DF-TEM image onto the original HRTEM image and d) the reconstructed DF image. The scale bars in images (c) and (d) are 5 nm.

The spontaneous exfoliation to monolayer nanosheets must be driven by the favorable solvation of the intercalated alkyl ether chains. Solvent swelling is expected to increase interlayer spacing, weaken the layer-layer interactions, and provide osmotic pressure to drive exfoliation; such a mechanism also supports the subsequent steric stabilization of the LZH colloidal solution by the carboxylate ligands.[31] The resulting solutions are stable to precipitation even by centrifugation (Figure S22, Supporting Information). The new method to deliver exfoliated nanosheets contrasts with anion exchange reactions and

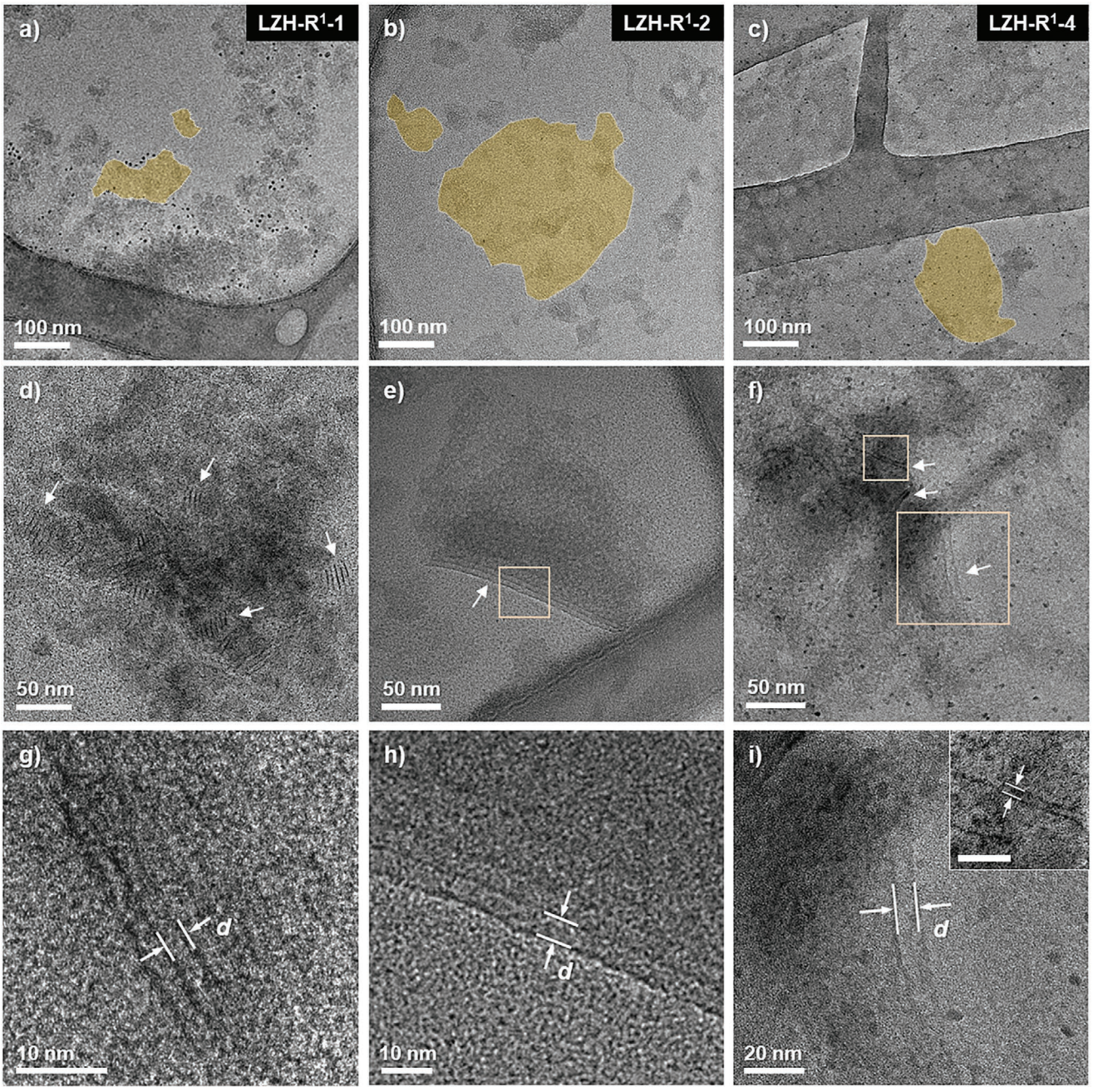

Figure 5. TEM images of exfoliated nanosheets (i.e., top-view along the *c*-axis) in a) LZH-R^1-1, b) LZH-R^1-2, and c) LZH-R^1-4. Individual nanosheets are outlined for clarity. TEM images showing evidence of stacking in d) LZH-R^1-1 (side-on), e) LZH-R^1-2 (tilted), and f) LZH-R^1-4 (tilted and side-on) and g) corresponding areas of measured basal spacings, h,i) magnified boxed regions. The inset in (i) is enlarged from the smaller box region in (f). The measured basal spacings (*d* values) are g) 2.53 ± 0.51 nm, h) 3.64 ± 2.35 nm, and i) 6.94 ± 1.24 nm, 3.58 ± 0.26 nm (inset), respectively.

achieves successful dissolution whilst avoiding energy intensive and structure damaging methods, as well as obviating toxic and high boiling solvents such as formamide.[26c,32]

2.4. Functional LZH Derivatives

The versatility of the organometallic synthesis method was further demonstrated using 5-hexenoic acid to introduce a vinyl group onto LZH-R^2. In addition to characteristic features observed in the XRD and FTIR spectrum (Figure 2), the successful LZH synthesis was further confirmed by ^{1}H NMR spectroscopy (Figure S23, Supporting Information). The broadening of all the carboxylate resonances and the absence of the free acid O—H resonance verify the formation of the LZH-R^2 compound. Moreover, resonances for the vinyl protons were observed at 5.61 and 4.93 ppm. The introduction of a terminal vinyl group provides an attractive site for a number of

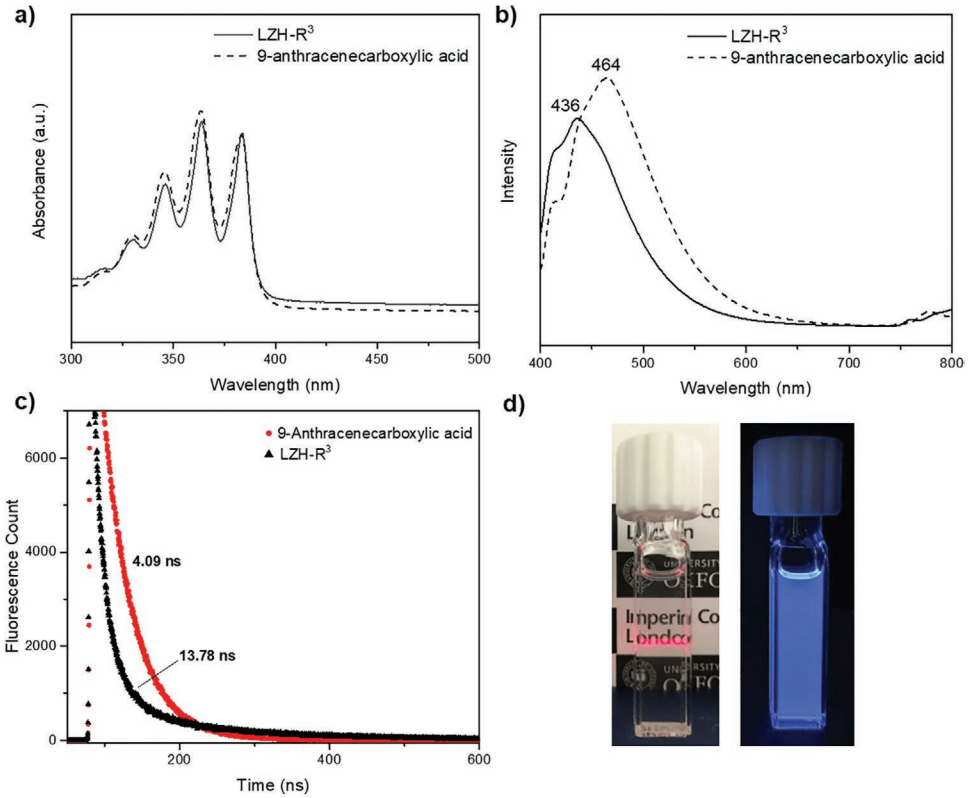

Figure 6. Photophysical characterization of LZH-R^3 compared to 9-anthracenecarboxylic acid at equivalent moieties a) UV–vis absorption spectra b) Excitation spectra λ_{exc} = 360 nm c) fluorescence lifetime decay d) Tyndall effect (left) and solution under UV illumination; LZH-R^3 (right).

post-synthetic modifications and the potential fabrication of surface functionalized thin-films.[33]

Another functional example is provided by the introduction of 9-anthracenecarboxylic acid via the direct synthesis of LZH-R^3, also confirmed by the XRD and FTIR measurements (Figure 2). The method easily accommodates the rigid and bulky anthracene moiety, in contrast to anion exchange methods which are generally limited to linear alkyl substituents. The intercalation of anthracene units can lead to either interactions between neighboring chromophores (i.e., π–π interactions) or interactions between the inorganic host and the chromophore, both influence the photophysical properties.[34] Comparing the UV–Vis spectra of LZH-R^3 with the free acid, at equivalent concentrations of anthracene in ethanol, shows similar features with characteristic absorptions at 300–400 nm assigned to anthracene (**Figure 6**a).[35] The fluorescence emission spectra are also identical with emission maxima at ≈360 nm (not shown here). However, the excitation spectra show a blue shift, from 464 to 436 nm, for the LZH-R^3, which is attributed to the intermolecular interactions between the excited anthracene moiety and the inorganic zinc hydroxide framework (Figure 6b).[36] Further evidence for the organized arrangement of anthracene groups within the LZH was obtained by time-resolved fluorescence data (Figure 6c). A fluorescence lifetime decay of 13.78 ns was observed for LZH-R^3 compared to that of the free acid with a lifetime of 4.09 ns. The longer lifetime is attributed to the more organized arrangement of anthracene moieties in the interlayer galleries of the LZH-R^3, which suppresses both thermal vibration and rotation of the anthracene anions.[37] Images of both the Tyndall scattering and fluorescence from LZH-R^3 further confirm the stable colloidal dispersion and retained fluorescent activity (Figure 6d).

3. Conclusions

A series of carboxylate intercalated LZHs were directly synthesized by the hydrolysis of diethyl zinc in the presence of carboxylic acids at room temperature. This new organometallic method provides an effective alternative to circuitous anion exchange reactions, obviates excess anion or surfactant usage and is free from common inorganic contaminants. A series of soluble LZH-R^1-n materials were prepared, using alkyl ether chains, which showed high solubility in polar solvents including alcohols and even in water. The maximum solubility values were an order of magnitude higher than previously reported. Importantly, the method efficiently delivers directly exfoliated nanosheets at high yields (70–80%), which are readily deposited as functional thin films, or converted to oxide under mild conditions. These materials, with their potentially high active surface areas, are particularly relevant to materials for energy conversion and storage applications. For example, the efficient and consistent incorporation of controlled polyether chain lengths in the interlayer spacing could provide a particularly useful strategy for layered electrode materials where large interlayer spacings are required to enhance ion diffusion.[38] Alternatively, the exfoliated LZHs could be used for drug delivery or aqueous biomedical sensing applications.[39] The synthesis is tolerant of functional carboxylic acids and was used to deliver

intercalates containing vinyl groups (LZH-R^2), suitable for post-synthetic modifications, or photoluminescent anthracene units (LZH-R^3) relevant for photoactive layered materials for use as detectors, UV-filters, or sensors. The new synthetic method may be more widely applied to the co-intercalation of multi-functional layered metal hydroxides, using mixed modifying ligands. By introducing additional organometallic precursors, there is scope to extend the method to doped LZHs or other functionalized LDHs. The controlled growth under mild conditions also offers unique opportunities to study the mechanisms of seeding, growth, and exfoliation, which may be broadly relevant to many useful 2D materials.

4. Experimental Section

Experimental Details: All syntheses were carried out under an inert atmosphere (N_2) using a glovebox and standard Schlenk line techniques. Toluene was obtained from a solvent purification system and was further degassed by freeze-thaw cycles and stored with molecular sieves (3 Å, Sigma Aldrich). Diethyl zinc (≥52 wt% Zn basis, Sigma Aldrich) was used as received. Methoxyacetic acid (98%, Sigma Aldrich) and 2-[2-(2-methoxyethoxy)ethoxy] acetic acid (technical grade, Sigma Aldrich) were distilled and degassed prior to use, whilst 2-(2-methoxyethoxy) acetic acid (98%, Fluorochem), 9-anthracenecarboxylic acid (>97%, TCI Chemicals), and 5-hexenoic acid (99%, Alfa Aesar) were used without further purification. 2,5,8,11,14-pentaoxaheptadecan-17-oic acid was synthesized according to the reported route and distilled before storing in a glovebox.[40]

Characterization: Powder XRD experiments were performed using a PANalytical Xpert Pro diffractometer, using a Cu Kα radiation source (λ = 0.154 nm) at 40 mA and 40 kV with a step size of 0.033° 2θ, scan step time of 70 s and scan range of 2–75° 2θ. Baseline corrections and line fittings were processed using Fityk Software (v 0.9.8). The average basal spacings were obtained from the (00l) using Bragg equation, λ = 2dsinθ. The average crystallite size (D) was estimated according to the Scherrer equation, $D = k\lambda/\beta\cos\theta$, where β is the full width at half maximum (FWHM) of the diffraction peak after instrumental broadening correction and k is the shape factor for the average crystallite. β is calculated from $\beta^2 = \beta_o{}^2 - b^{2,}$ where β_o is the measured FWHM of the sample and b is the measured FWHM of a well crystallized material (LaB_6, 99.5%, Alfa Aesar) to account for instrument broadening and k = 0.9 for powders, assuming spherical shape. FTIR spectra were obtained on a Bruker Tensor 27 spectrophotometer using 32 scans from 4000 to 600 cm^{-1} at a resolution of 4 cm^{-1}. TGA was performed on a Mettler Toledo TGA/DSC 1 STAR system using a temperature range of 30–800 °C at a heating rate of 10 °C min^{-1} using air with a flow rate of 100 mL min^{-1}. TGA-MS measurements were carried out on the same instrument integrated with a Hiden HPR-20 QIC EGA mass spectrometer. AFM samples were prepared by drop-cast (0.05 mg mL^{-1} solutions) on silicon wafers (Agar Scientifc) pre-cleaned using piranha solution. AFM imaging was carried out in dynamic mode on a hpAFM with AFM controller (NanoMagnetics Instruments, UK) using Nanosensor tapping mode probes. AFM micrographs were then processed with NMI Image Analyzer (v1.5, NanoMagnetics), with plane correction and scar removal using the in-built functions. The samples for SEM were mounted onto stubs using carbon tape and sputtered with a 10 nm layer of chromium. The SEM images were obtained on a Zeiss Auriga Cross Beam featuring a Schottky field emission gun with Gemini electron column at an accelerating voltage of 5 keV and a working distance of ≈7 mm. TEM samples were prepared by drop-casting diluted colloidal solutions (methanol, 0.05–0.01 mg mL^{-1}) onto ultrathin (≈3 nm) carbon films on lacy carbon support film, 300 mesh, gold TEM grids (Agar Scientific) and air dried. TEM images were acquired on a Cs aberration corrected Titan 80/300 TEM/STEM microscope operated at 80 kV and equipped with a Bruker XFlash EDS detector and Gatan Tridiem Giff. Virtual dark field images were generated by applying spatial masks at specific diffraction spots and then reconstructed into a dark-field image by inverse FFT process. The UV–vis absorption measurements were carried out on a Cary 4000 UV–vis spectrophotometer between 200 and 800 nm. The fluorescence emission and excitation spectra were obtained using a Cary Varian Eclipse Fluorescence Spectrophotometer in the range between 200 and 800 nm. Time-resolved fluorescence decay measurements were carried out on a Horiba Scientific Delta-Flex system configured with a 404 nm pulsed diode light (pulsed duration of <200 ps). A maximum repetition rate of 1.0 MHz and excitation pulse energy of 0.34 μ cm^{-2} was used for time-correlated single-photon counting measurements of transient photoluminescence referenced to a LUDOX solution. The transient fluorescent signal was collected using a standard single-photon counting detector (PPD-900, Horiba scientific). The samples under investigation were dispersed in EtOH solvent (at equivalent moieties of anthracene units) in quartz cuvettes with a 1 cm path length.

Synthesis: In a typical synthesis, diethyl zinc (2.74 mmol, 1.67 equiv.) was added dropwise to a suspension containing the carboxylic acid (1.64 mmol, 1.0 equiv.) in toluene (20 mL) and stirred (500 rpm) overnight at room temperature. The reaction mixture was then taken out of the glovebox and degassed water (4.34 mmol, 1.60 equiv. relative to zinc) was carefully added dropwise, under a nitrogen atmosphere and stirred for a further 3 h at room temperature. The resulting LZH was collected by centrifugation (2466 rcf, 30 min), followed by decanting the supernatant and drying the remaining solid under a reduced pressure. All LZHs were obtained in quantitative yields and used without further purification.

LZH-R^1-0. Synthesized using methoxyacetic acid. FT-IR ν_{max}/cm^{-1} 3438 (O—H, br), 2920 (C—H, br), 1589 (s; ν_{as}COO$^-$), 1412 (s; ν_sCOO$^-$), 1119 (CO—C, s). Anal. calcd for (Calc. for $C_6H_{18}O_{14}Zn_5$: C 11.24; H 2.83; found: C 11.2; H 2.6.

LZH-R^1-1. Synthesized using 2-(2-methoxyethoxy)acetic acid. FT-IR: 3422 (w; O—H), 2883 (s; C—H), 1585 (s; ν_{as}COO$^-$), 1414 (s; ν_sCOO$^-$), 1110 cm^{-1} (s; CO—C). Anal. calcd for $C_{10}H_{26}O_{16}Zn_5$: C 16.47, H 3.59; found: C 16.6, H 3.7.

LZH-R^1-2. Synthesized using 2-[2-(2-methoxyethoxy)ethoxy]acetic acid. FT-IR 3429 (w; O—H), 2876 (w; C—H), 1589 (s; ν_{as}COO$^-$), 1414 (s; ν_sCOO$^-$), 1103 cm^{-1} (s; CO—C). Anal. Calcd for $C_{21}H_{47}O_{23}Zn_5$: C 25.36, H 4.76; found: C 24.99, H 5.13.

LZH-R^1-4. Synthesized using 2,5,8,11,14-pentaoxaheptadecan-17-oic acid. FT-IR: 3440 (w; O—H), 2870 (w; C—H), 1570 (s; ν_{as}COO$^-$), 1430 (s; ν_sCOO$^-$), 1100 cm^{-1} (s; CO—C). Anal. calcd for $C_{36}H_{77}O_{29}Zn_5$: C 33.24, H 5.9; found: C 33.16, H 5.97.

LZH-R^2. Synthesized using 5-hexenoic acid. ^{1}H NMR (400 MHz, C_6D_6, δ) 5.75–5.52 (m, 1H), 5.05–4.82 (m, 2H), 2.22 (t, J = 7.5 Hz, 2H), 1.87 (q, J = 7.2 Hz, 2H), 1.69–1.49 (m, 2H). FT-IR: 3400 (w; O—H), 3078 (s; =C—H), 2935 (w; C—H), 1541 (s; ν_{as}COO$^-$), 1402 (s; ν_sCOO$^-$), 910 cm^{-1} (s; C=C). Anal. calcd for $C_{18}H_{35}O_{14}Zn_5$: C 26.95, H 4.40; found: C 29.30, H 4.67.

LZH-R^3. Synthesized using 9-anthracenecarboxylic acid and stored under inert conditions away from direct light. FT-IR: 3420 (w; O—H), 3050 (w; =C—H), 1546 (s; ν_{as}COO$^-$), 1430 cm^{-1} (s; ν_sCOO$^-$). Anal. Calcd for $C_{45}H_{35}O_{14}Zn_5$: C 47.97, H 3.13; found: C 50.23, H 3.44.

Dispersion and Exfoliation Treatment of LZH-R^1-n: The LZH-R^1-n (100–400 mg) were added into ethyl acetate, ethanol, methanol, or water (2–3 mL) and were gently stirred for 2 h at room temperature. The resulting saturated solutions were isolated from undispersed residuals after standing for 1 day. The saturation concentration or limiting solubility (mg mL^{-1}) of the LZH-R^1-n were determined from the corresponding weight of dried aliquots and the initial volume of the purified colloidal solution.

Supporting Information

Supporting Information is available from the Wiley Online Library or from the author.

Acknowledgements

The authors thank Shell Global Solutions Int. B.V. and the EPSRC (EP/S018603/1) for research funding.

Conflict of Interest

The authors declare no conflict of interest.

Data Availability Statement

Data available on request from the authors.

Keywords

2D nanosheets, exfoliation, intercalation, layered zinc hydroxides, organozinc

Received: March 17, 2021
Published online:

[1] a) C. Taviot-Guého, V. Prévot, C. Forano, G. Renaudin, C. Mousty, F. Leroux, *Adv. Funct. Mater.* **2018**, *28*, 1703868; b) C. Chen, L. Tao, S. Du, W. Chen, Y. Wang, Y. Zou, S. Wang, *Adv. Funct. Mater.* **2020**, *30*, 1909832; c) Y. Wang, D. Yan, S. El Hankari, Y. Zou, S. Wang, *Adv. Sci.* **2018**, *5*, 1800064; d) V. Nicolosi, M. Chhowalla, M. G. Kanatzidis, M. S. Strano, J. N. Coleman, *Science* **2013**, *340*, 1226419.

[2] W. Stählin, H. R. Oswald, *Acta Crystallogr. B* **1970**, *26*, 860.

[3] S. Inoue, S. Fujihara, *Inorg. Chem.* **2011**, *50*, 3605.

[4] a) A. Zięba, A. Pacuła, A. Drelinkiewicz, *Energy Fuels* **2010**, *24*, 634; b) D. M. Reinoso, D. E. Damiani, G. M. Tonetto, *Catal. Sci. Technol.* **2014**, *4*, 1803.

[5] T. Hongo, T. Iemura, S. Satokawa, A. Yamazaki, *Appl. Clay Sci.* **2010**, *48*, 455.

[6] a) J. Liu, X. Zhang, Y. Zhang, *ACS Appl. Mater. Interfaces* **2015**, *7*, 11180; b) A. C. T. Cursino, J. E. F. d. C. Gardolinski, F. Wypych, *J. Colloid Interface Sci.* **2010**, *347*, 49; c) J.-H. Yang, Y.-S. Han, M. Park, T. Park, S.-J. Hwang, J.-H. Choy, *Chem. Mater.* **2007**, *19*, 2679.

[7] a) T. Shinagawa, M. Watanabe, T. Mori, J.-i. Tani, M. Chigane, M. Izaki, *Inorg. Chem.* **2018**, *57*, 13137; b) R. Q. Song, A. W. Xu, B. Deng, Q. Li, G. Y. Chen, *Adv. Funct. Mater.* **2007**, *17*, 296; c) M. Sofos, J. Goldberger, D. A. Stone, J. E. Allen, Q. Ma, D. J. Herman, W. W. Tsai, L. J. Lauhon, S. I. Stupp, *Nat. Mater.* **2009**, *8*, 68.

[8] A. B. Djurišić, X. Chen, Y. H. Leung, A. Man Ching Ng, *J. Mater. Chem.* **2012**, *22*, 6526.

[9] Q. Wang, D. O'Hare, *Chem. Rev.* **2012**, *112*, 4124.

[10] M. Xu, M. Wei, *Adv. Funct. Mater.* **2018**, *28*, 1802943.

[11] U. Costantino, R. Vivani, M. Bastianini, F. Costantino, M. Nocchetti, *Dalton Trans.* **2014**, *43*, 11587.

[12] a) N. Candu, D. Paul, I.-C. Marcu, M. Tudorache, V. I. Parvulescu, S. M. Coman, *Inorg. Chim. Acta* **2018**, *475*, 127; b) S. Aisawa, S. Takahashi, W. Ogasawara, Y. Umetsu, E. Narita, *J. Solid State Chem.* **2001**, *162*, 52; c) E. Gardner, K. M. Huntoon, T. J. Pinnavaia, *Adv. Mater.* **2001**, *13*, 1263; d) G. Hu, N. Wang, D. O'Hare, J. Davis, *Chem. Commun.* **2006**, 287.

[13] a) C. Amiens, B. Chaudret, D. Ciuculescu-Pradines, V. Collière, K. Fajerwerg, P. Fau, M. Kahn, A. Maisonnat, K. Soulantica, K. Philippot, *New J. Chem.* **2013**, *37*, 3374; b) D. Prochowicz, K. Sokołowski, J. Lewiński, *Coord. Chem. Rev.* **2014**, *270–271*, 112; c) J. A. Garden, S. D. Pike, *Dalton Trans.* **2018**, *47*, 3638.

[14] a) S. D. Pike, E. R. White, M. S. P. Shaffer, C. K. Williams, *Nat. Commun.* **2016**, *7*, 13008; b) K. L. Orchard, M. S. P. Shaffer, C. K. Williams, *Chem. Mater.* **2012**, *24*, 2443; c) M. L. Kahn, M. Monge, V. Collière, F. Senocq, A. Maisonnat, B. Chaudret, *Adv. Funct. Mater.* **2005**, *15*, 458; d) M. Monge, M. L. Kahn, A. Maisonnat, B. Chaudret, *Angew. Chem., Int. Ed.* **2003**, *42*, 5321.

[15] a) W. Bury, E. Krajewska, M. Dutkiewicz, K. Sokołowski, I. Justyniak, Z. Kaszkur, K. J. Kurzydłowski, T. Płociński, J. Lewiński, *Chem. Commun.* **2011**, *47*, 5467; b) M. L. Kahn, A. Glaria, C. Pages, M. Monge, L. Saint Macary, A. Maisonnat, B. Chaudret, *J. Mater. Chem.* **2009**, *19*, 4044.

[16] A. H. M. Leung, S. D. Pike, A. J. Clancy, H. C. Yau, W. J. Lee, K. L. Orchard, M. S. P. Shaffer, C. K. Williams, *Chem. Sci.* **2018**, *9*, 2135.

[17] D. McManus, S. Vranic, F. Withers, V. Sanchez-Romaguera, M. Macucci, H. Yang, R. Sorrentino, K. Parvez, S.-K. Son, G. Iannaccone, K. Kostarelos, G. Fiori, C. Casiraghi, *Nat. Nanotechnol.* **2017**, *12*, 343.

[18] K. L. Orchard, A. J. P. White, M. S. P. Shaffer, C. K. Williams, *Organometallics* **2009**, *28*, 5828.

[19] A. V. Radha, P. Vishnu Kamath, G. N. Subbanna, *Mater. Res. Bull.* **2003**, *38*, 731.

[20] S. Carlino, *Solid State Ion.* **1997**, *98*, 73.

[21] a) J. Yu, Q. Wang, D. O'Hare, L. Sun, *Chem. Soc. Rev.* **2017**, *46*, 5950; b) C. Liang, Y. Shimizu, M. Masuda, T. Sasaki, N. Koshizaki, *Chem. Mater.* **2004**, *16*, 963.

[22] a) Y. Kong, Y. Huang, C. Meng, Z. Zhang, *RSC Adv.* **2018**, *8*, 31440; b) P. Li, F. Lv, Z. Xu, G. Qi, Y. Zhang, *J. Mater. Sci.* **2013**, *48*, 5437.

[23] F. Song, X. Hu, *Nat. Commun.* **2014**, *5*, 4477.

[24] J. Miao, M. Xue, H. Itoh, Q. Feng, *J. Mater. Chem.* **2006**, *16*, 474.

[25] a) O. Altuntasoglu, Y. Matsuda, S. Ida, Y. Matsumoto, *Chem. Mater.* **2010**, *22*, 3158; b) J. W. Lee, W. C. Choi, J.-D. Kim, *CrystEngComm* **2010**, *12*, 3249.

[26] a) V. V. Naik, T. N. Ramesh, S. Vasudevan, *J. Phys. Chem. Lett.* **2011**, *2*, 1193; b) N. Iyi, Y. Ebina, T. Sasaki, *J. Mater. Chem.* **2011**, *21*, 8085; c) R. Ma, Z. Liu, L. Li, N. Iyi, T. Sasaki, *J. Mater. Chem.* **2006**, *16*, 3809; d) T. Hibino, *Chem. Mater.* **2004**, *16*, 5482.

[27] G. V. Manohara, L. Li, A. Whiting, H. C. Greenwell, *Dalton Trans.* **2018**, *47*, 2933.

[28] L. Zhao, J. Miao, Y. Iwasa, Q. Feng, *J. Ceram. Soc. Jpn.* **2008**, *116*, 657.

[29] a) C. Schliehe, B. H. Juarez, M. Pelletier, S. Jander, D. Greshnykh, M. Nagel, A. Meyer, S. Foerster, A. Kornowski, C. Klinke, H. Weller, *Science* **2010**, *329*, 550; b) Q. Zhang, S.-J. Liu, S.-H. Yu, *J. Mater. Chem.* **2009**, *19*, 191; c) N. A. Jose, H. C. Zeng, A. A. Lapkin, *Nat. Commun.* **2018**, *9*, 4913.

[30] a) Z. P. Xu, P. S. Braterman, K. Yu, H. Xu, Y. Wang, C. J. Brinker, *Chem. Mater.* **2004**, *16*, 2750; b) J. Demel, J. Plestil, P. Bezdicka, P. Janda, M. Klementova, K. Lang, *J. Colloid Interface Sci.* **2011**, *360*, 532.

[31] Z. Liu, R. Ma, M. Osada, N. Iyi, Y. Ebina, K. Takada, T. Sasaki, *J. Am. Chem. Soc.* **2006**, *128*, 4872.

[32] Q. Wu, A. Olafsen, Ø. B. Vistad, J. Roots, P. Norby, *J. Mater. Chem.* **2005**, *15*, 4695.

[33] O. Palamarciuc, E. Delahaye, P. Rabu, G. Rogez, *New J. Chem.* **2014**, *38*, 2016.

[34] L. Latterini, M. Nocchetti, G. G. Aloisi, U. Costantino, F. Elisei, *Inorg. Chim. Acta* **2007**, *360*, 728.

[35] L. Latterini, M. Nocchetti, G. G. Aloisi, U. Costantino, F. C. De Schryver, F. Elisei, *Langmuir* **2007**, *23*, 12337.

[36] D. Yan, J. Lu, M. Wei, D. G. Evans, X. Duan, *J. Mater. Chem.* **2011**, *21*, 13128.

[37] a) W. Shi, Z. Sun, M. Wei, D. G. Evans, X. Duan, *J. Phys. Chem. C* **2010**, *114*, 21070; b) G. Wang, S. Xu, C. Xia, D. Yan, Y. Lin, M. Wei, *RSC Adv.* **2015**, *5*, 23708.
[38] Y. Zhang, E. H. Ang, Y. Yang, M. Ye, W. Du, C. C. Li, *Adv. Funct. Mater.* **2021**, *31*, 2007358.
[39] a) D. Yan, J. Lu, M. Wei, J. Han, J. Ma, F. Li, D. G. Evans, X. Duan, *Angew. Chem., Int. Ed.* **2009**, *48*, 3073; b) M. Adewoyin, S. M. N. Mohsin, P. Arulselvan, M. Z. Hussein, S. Fakurazi, *Drug Des., Dev. Ther.* **2015**, *9*, 2475.
[40] J. Kubitschke, S. Javor, J. Rebek Jr., *Chem. Commun.* **2012**, *48*, 9251.